

# Formation control of robots in nonlinear two-dimensional potential

Yanran Wang Tatsuya Baba Takashi Hikiyara  
Department of Electrical Engineering, Kyoto University

April 21, 2023

## Abstract

The formation control of multi-agent systems has garnered significant research attention in both theoretical and practical aspects over the past two decades. Despite this, the examination of how external environments impact swarm formation dynamics and the design of formation control algorithms for multi-agent systems in nonlinear external potentials have not been thoroughly explored. In this paper, we apply our theoretical formulation of the formation control algorithm to mobile robots operating in nonlinear external potentials. To validate the algorithm's effectiveness, we conducted experiments using real mobile robots. Furthermore, the results demonstrate the effectiveness of Dynamic Mode Decomposition in predicting the velocity of robots in unknown environments.

## 1 Introduction

Multi-Agent Systems (MAS) are systems in which the global objective is achieved through local interactions among a group of simple agents. In the field of swarm robotics, researchers aim to understand existing MAS in nature, such as bird flocking, by formulating them as dynamical systems [1–6]. Additionally, they construct artificial robot-based MAS for a wide range of applications [7–11]. Due to the constraint of the complexity of individuals in MAS, agent acts autonomously based on only local perception and coordination with their neighbors. As a result, with limited sensing and communication capabilities, MAS naturally maintains formation as a group.

Swarm formation is often observed in natural MAS, which has inspired researchers with the development of formation control algorithms for artificial swarms. Recent advances in swarm robotics have presented various successful implementations of swarm formation control for both centralized and decentralized approaches. However, these studies generally treat swarm formation control as a standalone problem [5, 6, 12–15]. Most of the research focuses on maintaining formation in the presence of obstacles in a steady environment, while not much attention is paid to the formation dynamics shaped by an nonlinear

environments. On the other hand, when swarm robotics applied in unknown environment mapping tasks [16, 17], swarm formation appears only as a byproduct of maximizing coverage area while maintaining agent-to-agent connections.

In our previous study [18], we formulated algorithms that obtain desired environmental information by analyzing changes in sensor swarm formations, rather than through direct data collection by individual sensors. We identify the environmental information as an external potential hyperspace  $M$  of  $(n - 1)$ -dimensions. We defined the swarm formation using the geodesic deviation equation and used Koopman operator theory [19–21] and Dynamic Mode Decomposition (DMD) [22] to predict the state of the nonlinear autonomous dynamical system of individual agents in the swarm in order to maintain the desired formation.

In this study, we performed experiments to validate the designed algorithms for formation control. We used two omnidirectional mobile robots, one serving as the leader and the other as the follower, each equipped with a visual system and a sensing system. The experiment was conducted on an elliptic paraboloid potential. We designed visual and velocity prediction algorithms that enable the robots to maintain the defined formation while navigating on the nonlinear external potential. The formation control algorithm is easily scalable to accommodate additional follower robots in the formation.

This paper is organized as the follows. Section 2, we introduce the mathematical definition of the formation and demonstrate how to construct such formation in an arbitrary external potential both in theory and in experiment. For Section 3, we explain the experimental setups, including specification of the external potential, and the hardware specifications of the mobile robot. In Section 4, we formulate the algorithm which guides the individual robot to stay in formation as it moves in the external potential. Section 5 we present and discuss on the experimental results with mobile robots. Finally, Section 6 concludes the paper.

## 2 Methodology

### 2.1 Formation definition

The topology of the formation follows [18], which is line formation. Mathematically, we define a *path graph*  $P_n$  as a pair  $(\mathcal{V}, \mathcal{E})$  that consists of a set of vertices  $\mathcal{V} = \{v_1, v_2, \dots, v_n\}$  and a set of edges  $\mathcal{E}$  such that  $\mathcal{E} \subseteq \{v_i, v_{i+1}\}$ , where  $i = 1, 2, \dots, n - 1$ . Each vertex represents an individual robot, while the edges represent the distance between any two neighbouring robots. To define the edges unambiguously, let  $q = (q_1, \dots, q_n)^T$  be the configuration of all robots, where  $q_i \in \mathbb{R}$  denote the position of robot  $v_i$  for all  $v_i \in \mathcal{V}$ . The length of edges,  $dis(\mathcal{E})$ , is defined to be the geodesic distance between two connected vertices over  $P_n(q)$ .

To stay in the desired formation, all robots are to maintain an identical

inter-robot distance. Thus we force an algebraic constraint on the edges,

$$dis(\mathcal{E}_{v_i, v_{i+1}}) = d, \quad \forall v_i \in V, \quad d \in \mathbb{R}. \quad (1)$$

The robots are classified into two types: leaders and followers. The leader robot follows a predefined trajectory, which serves as the initial stimulus for the entire formation. The followers use their neighboring robots as beacon robots, selecting the one closest to the leader robot, and maintain a constant relative distance with this beacon robot.

In flat space, or mathematically in  $\mathbb{R}^2$ , the relative distance between each pair of robots is measured along the line that is normal to the velocity of the beacon robot in Euclidean metric. Naturally, observed from the ambient space  $\mathbb{R}^3$ , the desired formation is a straight line that is normal to the velocity of the head robot at each given timesteps, with each follower robots keeping identical relative Euclidean distances. Consequently, the trajectories of the follower robots are to be parallel lines to the leader robot.

In curved space, or mathematically in any arbitrary two-dimensional external potential  $M$ , by definition, the edge representation of the formation is a parallel vector field that is metrically orthogonal to the head agent trajectory, with each follower robots separated by identical proper time. Since the edges are metric-dependent, observed from the ambient space  $\mathbb{R}^3$ , the trajectories of the follower robots are no longer parallel to the leader robots.

## 2.2 Problem Formulation

### 2.2.1 Mathematical construction of the formation

Given the trajectory of leader robot, the trajectory of the follower robot can be constructed base on the definition of desired formation [23, 24].

The trajectory of the leader robot is pre-defined to be a geodesic curve on the manifold. Although any arbitrary trajectory can be used, this choice of leader robot trajectory is made to simplify dynamic control. On the geodesic curve, the leader robot travels with a constant velocity given its initial position and velocity, thus eliminating the need for an outside reference beacon. For a two-dimensional manifold  $(M, g)$ , leader robot trajectory  $l(t)$  can be expressed as a system of ordinary differential equations

$$\begin{aligned} \dot{l}_1 &= l_3, \\ \dot{l}_2 &= l_4, \\ \dot{l}_3 &= -\Gamma_{\mu\mu}^{\mu}(l_3)^2 - 2\Gamma_{\mu\nu}^{\mu}l_3l_4 - \Gamma_{\nu\nu}^{\mu}(l_4)^2, \\ \dot{l}_4 &= -\Gamma_{\mu\mu}^{\nu}(l_3)^2 - 2\Gamma_{\mu\nu}^{\nu}l_3l_4 - \Gamma_{\nu\nu}^{\nu}(l_4)^2, \end{aligned} \quad (2)$$

where basis  $\{\mu, \nu\}$  are used in the index,  $\dot{l}$  are the first derivative with respect to time, and  $\Gamma$  are the Christoffel symbols. (See section A for mathematical details)

The distance of the edges of desired formation needs to be identical in terms of the potential metric. For edges representation, a parallel vector field  $K$  that is orthogonal to the leader robot trajectory  $l(t)$  is constructed as

$$\nabla_K K = 0. \quad (3)$$

$K$  forms a family of geodesics where the initial position and velocity conditions  $(u_0^j, v_0^j)$  for  $j$ th geodesic  $\gamma_j \in K$  are  $u_0^j = l(t_j)$ ,  $v_0^j = v$ , such that  $g(v, \dot{l}(t_j)) = 0$ ,  $j \in \mathbb{Z}$ .

The separation vector  $s(t)$  connects a point  $\gamma(t)$  on one geodesic to a point  $\gamma(t) + s(t)$  on a nearby geodesic at the same proper time. For parallel vector field  $K$ , we can construct a separation vector field  $S$  such that  $s \in S$  are the separation vector described above. The follower robots' trajectories are the integral curves of  $S$ .

### 2.2.2 Experimental construction of the formation

For the experiment, the leader robot is defined to travel on a geodesic curve. To maintain a constant velocity, we require the leader robot to maintain a preset wheel rotation for all four wheels in each given timestep.

The trajectory of the follower robot, as stated in Section 2.2.1, requires knowledge of the metric of the arbitrary potential  $M$ . However, in the experiment, this metric is unknown to all robots. Therefore, we assume that the inter-robot distance can be approximated locally using the Euclidean metric. Thus, we require the follower robot to detect its relative distance and angle to its beacon neighbor.

Unlike in the mathematical construction, the robots in the experiment are no longer point elements. Robot-to-robot relative angle and position, as well as robot velocity, are determined with respect to the center point of the robot, as shown in Fig. 1.

## 3 Hardware Design

### 3.1 Design of external potential

We choose the external potential  $M$  to be a two-dimensional elliptic paraboloid, which can be explicitly represented as  $\frac{1}{40000}(x_1^2 + x_2^2) - x_3^2 = 0$ . Fig. 2 shows a photo of the external potential. A fence cover is build around the potential to reduce inteference with the robots' visual system.

### 3.2 Design of robot

The external view of the robot is shown in Fig. 3. The robot is modified based on OSOYOO® Model ZZ012318MC Metal Chassis Mecanum Wheel. It is 365mm in length, 238mm in width, 216mm in height, and weighs 1700 grams. We define the longer side to be the v-axis of the robot, while the shorter side

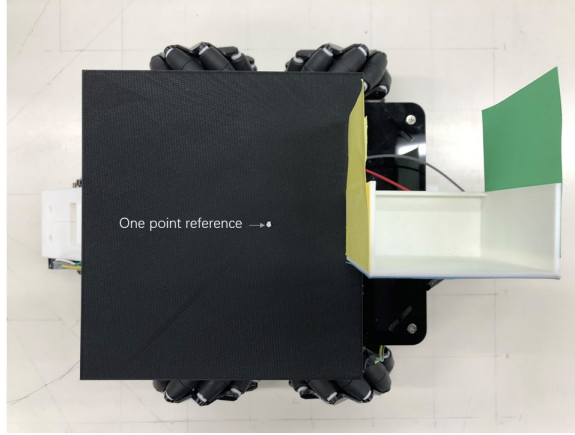


Figure 1: Robot with body cover. The white dot is set as the one-point position reference for the robot.

is the u-axis. Besides the metal and acrylic skeletons, the robot has three main system: movement system, sensing and storage system, and visual system, all connects to the central processing unit, Arduino Due. A body cover is made to reduce the interference for the visual system, and also acts as a one-point reference for the observer as shown in Fig. 1.

### 3.2.1 Movement system

The movement system is responsible for robot's mobility. The system consists of OSOYOO® Model-X Motor Driver Module, 18650 battery, DC encoder motor, and Mecanum wheels.

**Driver module** The OSOYOO® Model-X motor driver module is an improved L298N module. Two motor driver modules are used to control the front wheels and the rear wheels, respectively.

**18650 battery** The pair of battery acts as the power supply for the whole robot.

**DC encoder motor** There are four DC encoder motors in the robot, corresponding to the four wheels. Each motor consists of two parts: a GM25 DC motor and a dual-channel encoder. The dual-channel encoder can measure wheel rotations of the robot, allowing it to be programmed to travel a preset distance by specifying the number of wheel rotations.

**Mecanum wheel** The Mecanum wheel is an omnidirectional wheel, made with various rubberized rollers obliquely attaching to the wheel rim [25]. With a

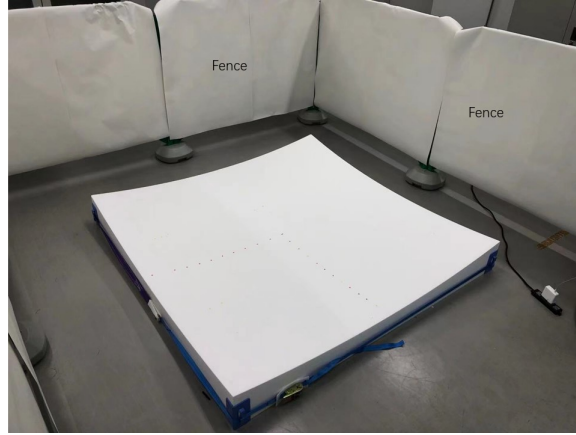


Figure 2: External potential view. The potential is made of polystyrene foam. It is 1780mm by 1780mm, with minimal height 50mm, and maximum height 208.4mm. See section B for more specification of the potential.

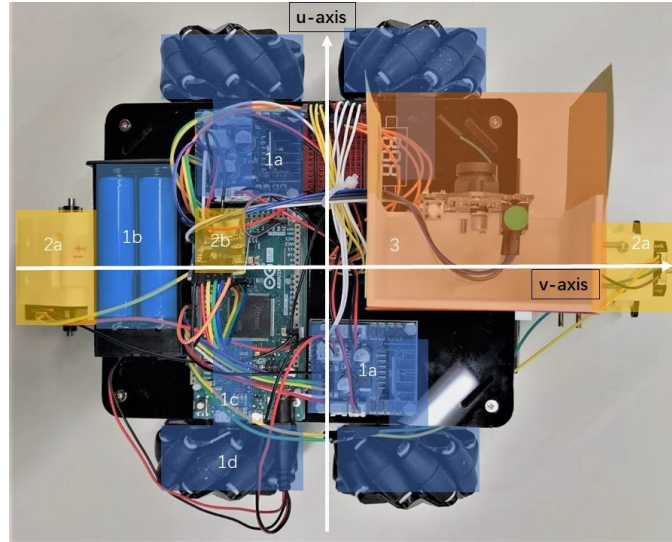


Figure 3: Robot external view. Movement system, sensing and storage system, and visual system are labeled in blue, yellow and orange, respectively. Numerical label indicates respective Section for parts descriptions.

combination of different wheel driving direction, movements to various directions can be performed. Fig. 4 demonstrates the relationship between wheel rotation directions and robot moving directions.

"In an ideal condition, all robots would have the same wheel rotation-to-

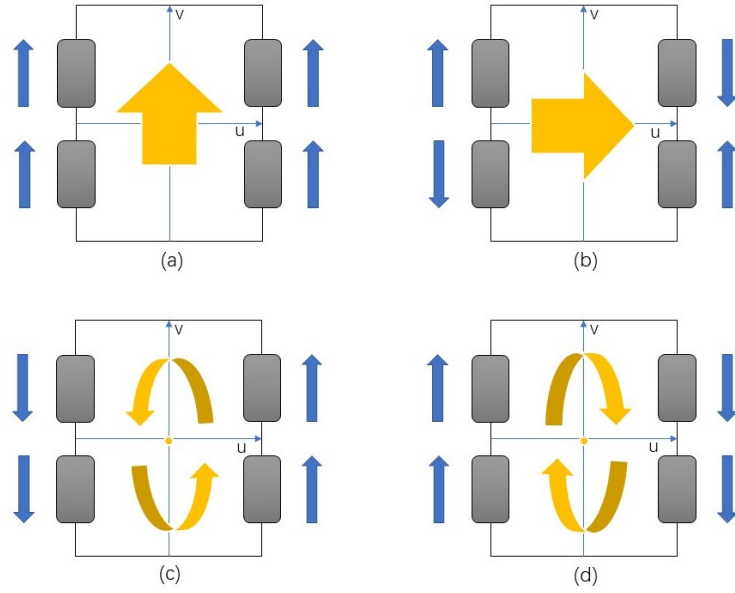


Figure 4: The movement scheme of robot. Blue arrow represents the rotation direction of the wheels, yellow arrow represents movement direction of the robot. Four types of movement are used in the experiment: (a) along  $v$ -axis of robot. (b) along  $u$ -axis of robot. (c) counterclockwise rotation. (d) clockwise rotation.

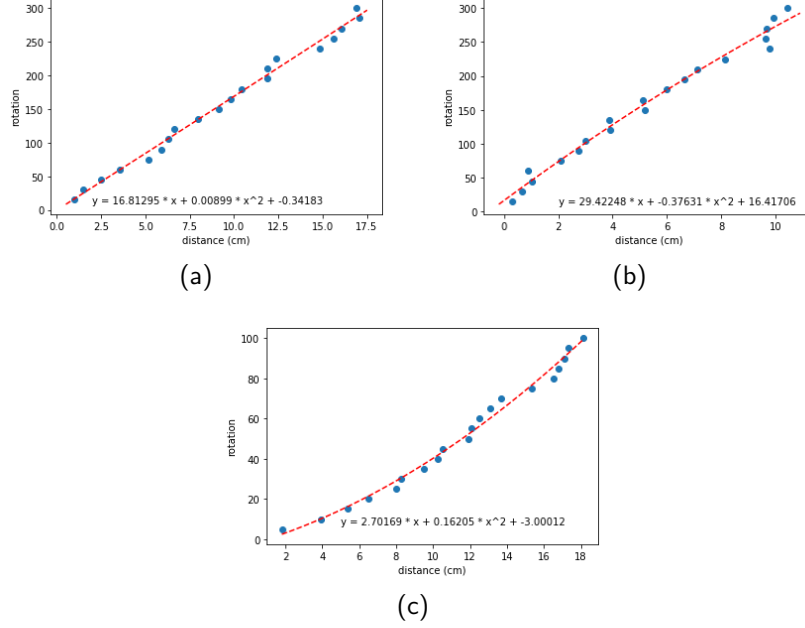


Figure 5: Motor calibration functions. (a) Movement along v-axis for follower robot. (b) Movement along u-axis for follower robot. (c) Movement along v-axis for leader robot.

distance conversion function. However, due to the instability and limited accuracy of motors, this conversion function varies for each individual robot. To rectify this, both leader and follower robots are calibrated based on their own distance-to-wheel rotation function, as shown in Fig. 5. The motor calibration function is obtained by curve fit the travelled distance measured by observer using one-point reference for various wheel rotations. With the restriction of the size of the external potential and the size of robots using for the experiment, we have focused on finetuning the robots with travelling distance under 20 cm along v-axis, and 10 cm along u-axis. Note the leader robot only calibrated for movement along v-axis, since it only requires to travel in that direction.

### 3.2.2 Sensing and storage system

The sensing and storage system is responsible for measuring and recording robot's velocity (per given timesteps) along its  $u$  and  $v$  axis.

**Sensing system** The sensing system is illustrated in Fig. 6. The system is implemented for both v-axis and u-axis. It consists of supporting platform, AMT102-V encoder with configuration 512 resolution and 15000 maximum RPM, and 38mm double aluminum omni wheel. This system is necessary to



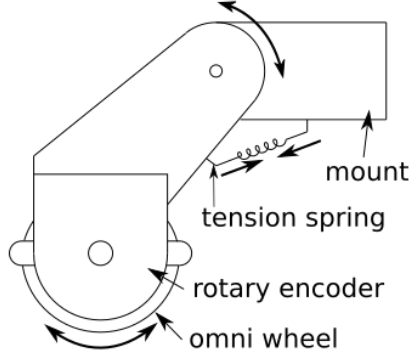


Figure 6: Scheme of robot’s sensing system. The sensing system is mounted on the robot’s metal skeleton through its supporting platform. The tension spring allows the omni wheel to keep in contact with the potential surface while travelling.

improve the accuracy of velocity measurement, as the encoder on the DC motor is affected by the swiping motion of the robot. Fig. 7 demonstrate the travelled distance measured by sensing system, and by observer using one-point reference for different travelling distance. The sensing system has provided reliable data for the actual velocities of the robot, which is crucial for the velocity prediction algorithm in section 4.3.

**Storage system** We use a SD card module and 8GB SD card to collect robot’s data, such as velocity, current timesteps, and number of movements. However, the storage system is solely for the experimental data analysis. The formation algorithm of the robots do not require such data collection.

### 3.2.3 Visual system

The visual system consists Pixy2 Camera with supporting pillar and square color papers, as shown in Fig. 8. The square color papers are of side length 70 mm, and are in three different colors, named front, rear and target color signature.

The visual system has two main objectives, calculate relative angle, and relative distance between the follwer robot and its beacon neighbor.

## 4 Algorithms

The leader robot is programmed to travel along its v-axis for a constant velocity per given timestep. The follower robot algorithm is shown in Fig. 9. The data collecting phase is requested for the velocity prediction algorithm. In data collecting phase, the predicted velocity of timestep  $k + 1$  is the final velocity of

timestep  $k$ . The follower robot algorithm has three sub-algorithm: the movement algorithm is responsible for executing the predicted velocity for each given timesteps; the visual algorithm is responsible for correcting the relative position and angle of the follower robot to its beacon neighbour; the velocity prediction algorithm is responsible for velocity prediction using data of previous velocities.

#### 4.1 Movement algorithm

The movement algorithm converts predicted distance  $(v_p, u_p)$  to wheel rotations of movement along robot's u-axis and v-axis according to each robot's own motor calibration function presented in section 3.2.1. During each movement, external encoder measure and records the actual travelled distance.

#### 4.2 Visual algorithm

The Pixy2 camera detects color blocks and labels them with their respective color signature. The final objective of the follower robot is to achieve a predefined relative position and angle with respect to its beacon neighbour, using the one-point reference.

In order to understand the relationship between Pixy2 image data and robots' relative position and angle, we set the beacon neighbour's position to be at the origin,  $(0, 0)$ , and use it as the reference point. We consider a relative distance between the follower robot and its beacon neighbour of  $\pm 45$  cm along the u-axis, and  $\pm 45$  cm along the v-axis. Image data of Pixy2, including block color signature, block position, and block width and height, are captured every 5 cm. When follower robot's v-axis is parallel to its beacon neighbour, it is considered to have zero relative angle. The relative angle becomes positive in the clockwise direction of the follower robot, with the beacon neighbour taken as the frame of reference. For each position, nine different relative angle,  $\pm 60^\circ, \pm 45^\circ, \pm 30^\circ, \pm 15^\circ, 0^\circ$  are also considered. For specific parameters of Pixy2 setting see section C.

Based on Fig. 10, which is the overlaid image data of all relative angles, we define four areas. The Unattainable area is shown in red, indicating the positions that the follower robot cannot reach due to the volume of robots. The green Front area always captures at least the front color signature block. The blue Target area only captures the target color signature block. The yellow Rear area always captures at least the rear color signature block. The visual algorithm utilizes image data from the Pixy2 camera to determine the movements taken by the follower robot. Its design is intended to guide the follower robot to first reach the Target area and then fine-tune its relative position and angle to achieve the final desired position.

We briefly summarize the visual algorithm for attaining Target area. The follower robot begins by checking the number of color blocks detected by the Pixy2 sensor. Four cases are considered: when one or two blocks are detected, the follower robot checks the color signature of the blocks and moves along the u-axis and v-axis accordingly; when more than two blocks are detected, the

follower robot moves along the u-axis and away from its beacon neighbour; when zero blocks are detected, the follower robot stops. Fig. 11 (in red background) shows the detailed visual algorithm flow. Notice that all movements in the algorithm is taking robot itself as the frame of reference.

Once the follower robot reaches the Target area, fine-tuning movements are necessary. Shown in Fig. 11 (in blue background), Target color signature block's position, width, and height are used for the finetuning process. We first adjust the position of the Target color signature block, which determines the relative position of the follower robot and its beacon neighbor along the v-axis, (Fig. 12), then adjust the block's area, which determines the relative distance along u-axis (Fig. 13).

Since when adjusting position along v-axis, the follower robot do not have information about its relative position along u-axis, we finetune along v-axis in the range of  $(-3, 3)$ , where the difference in pan functions between various u-axis distance is small (less than 7 pixel). The finetuning process tolerants small error (section D) in color signature block's side length difference, u-axis position and v-axis position due to unavoidable flickering of the Pixy2 camera.

### 4.3 Velocity prediction algorithm

To stay in formation as the robots travelling through external potential, individual robot needs dynamic control of its trajectory. However, the visual system provides only a limited sensing area for the follower robot to adjust its position and angle. To achieve higher accuracy and efficiency in tracking its beacon neighbor, a velocity prediction algorithm is required for the follower robot.

#### 4.3.1 Koopman operator theory and Online Dynamic Mode Decomposition

In the experiment, we consider the robot's trajectory to be a discrete-time dynamical system,

$$\mathbf{z}_{k+1} = \mathbf{F}(\mathbf{z}_k), \quad (4)$$

where  $\mathbf{z}_k$  is the sampling of the state of the system, that is the position of the robot, and  $\mathbf{F}$  is a vector field depends on the system dynamics. Due to the curvature property of the external potential manifold, the trajectories of robots are essentially nonlinear. To analyze nonlinear dynamic with linear technique, we utilize Koopman operator theory and Dynamic Mode Decomposition.

Koopman theory has demonstrated that a nonlinear dynamical system can be represented by an infinite-dimensional linear operator that operates on a Hilbert space of measurement functions of the system's state. The basic elements of Koopman spectral analysis is discussed in [19–21]. For systems with unknown governing equation, such as in our situation, Dynamic Mode Decomposition (DMD) algorithm is adopted to approximates the Koopman operator [18, 22].

We consider a sequential set of data vectors  $\{\mathbf{x}_0, \mathbf{x}_1, \dots, \mathbf{x}_m\}$ , where each  $\mathbf{x}_k \in \mathbb{R}^n$ , are some measurements of the system states of time  $t_0$  to  $t_m$ . These

data can be arranged into two matrices

$$\mathbf{A} = \begin{bmatrix} | & | & & | \\ \mathbf{x}_0 & \mathbf{x}_1 & \dots & \mathbf{x}_{m-1} \\ | & | & & | \end{bmatrix}, \quad \mathbf{B} = \begin{bmatrix} | & | & & | \\ \mathbf{x}_1 & \mathbf{x}_2 & \dots & \mathbf{x}_m \\ | & | & & | \end{bmatrix}. \quad (5)$$

We assume there exist an operator  $\mathbf{T}$  that approximates the nonlinear dynamic of the system as

$$\mathbf{x}_{k+1} \approx \mathbf{T}\mathbf{x}_k. \quad (6)$$

Then the best-fit operator  $\mathbf{T}$  is defined as

$$\mathbf{T} = \arg \min_{\mathbf{T}} \|\mathbf{B} - \mathbf{T}\mathbf{A}\|_F, \quad (7)$$

where  $\|\cdot\|_F$  is the Frobenius norm. The unique solution to least-square problem is given by

$$\mathbf{T} = \mathbf{B}\mathbf{A}^\dagger, \quad (8)$$

where  $\mathbf{A}^\dagger$  denotes the Moore-Penrose pseudoinverse of  $\mathbf{A}$ .

Online DMD algorithm updates operator  $\mathbf{T}$  for every timesteps, providing a more reliable operator  $\mathbf{T}$  for the prediction of future system states. The algorithm computes  $\mathbf{T}_{k+1}$  given  $\mathbf{T}_k$  and new pairs of data  $(a_{k+1}, b_{k+1}) \equiv (\mathbf{x}_k, \mathbf{x}_{k+1})$ , on the assumption that  $\mathbf{T}_{k+1}$  is close to  $\mathbf{T}_k$  in some sense.

#### 4.3.2 Online DMD Algorithm

After the data collecting phase, Online DMD algorithm shown below is used to predict the velocity of the next timestep. For mathematical details, see section E.

The steps taken in Online DMD algorithm is summarized as follows,

1. Arrange the collected robot's velocities  $x_k$  at each given timesteps into two matrices

$$\mathbf{A} \equiv [x_0 \ x_1 \ x_2], \quad \mathbf{B} \equiv [x_1 \ x_2 \ x_3].$$

2. Compute  $\mathbf{T}_k$  and  $(\mathbf{A}_k \mathbf{A}_k^T)^{-1}$  according to eq. (7).
3. Predict  $\mathbf{x}_{k+1}$ .
4. Correcting of  $\mathbf{x}_{k+1}$  by visual algorithm.
5. Update  $\mathbf{T}_k$  and  $(\mathbf{A}_k \mathbf{A}_k^T)^{-1}$  using corrected data pair  $(\mathbf{x}_k, \mathbf{x}_{k+1})$ .

## 5 Experiment and Discussion

### 5.1 Experimental results

For the experiment, one leader robot and one follower robot is used. The leader robot is set to travel 5 cm for each given timesteps. The follower robot has an

initial velocity equivalent to that of the leader robot, and it uses the algorithm described in section 4.

Two tracks are chosen. Track one runs horizontally on the external potential, with 15 timesteps, while track two runs diagonally with 20 timesteps. The initial position of the leader robot is predefined, while the follower robot is placed at 32 cm away in the v-axis, 0 cm in the u-axis, with zero angle, relative to the leader robot. Camera is located above the center point of the external potential, and photos are taken for each movement of the robots to obtain their trajectories. For both track, two types of algorithm is used. Figs. 14 (a) and (c) use DMD algorithm to predict next timestep velocity, while for Figs. 14 (b) and (d), the velocity from the preceding time step is utilized, and is named non-DMD velocity prediction.

Overall, the algorithm used by the follower robot was successful in tracking the leader robot on both tracks. Although in track two, without using the DMD prediction algorithm, the follower robot lost sight of the leader robot in the final time step, the visual algorithm demonstrated its capability in adjusting the relative position and angles, even when the prediction was less than ideal. (at timestep 14).

To examine the difference between follower robot's algorithm with DMD prediction and without DMD prediction, the correction distance in the visual algorithm stage is compared as shown in Fig. 15. In total, the correction distance of follower robot's algorithm with DMD prediction is 147% of algorithm without DMD prediction for track one, and 22% for track two.

## 5.2 Discussion

### 5.2.1 On DMD prediction algorithm

Online DMD algorithm used for velocity prediction assumes there is a linear operator advances some measurement functions (velocity) of the nonlinear system state (position of the follower robot). To find this linear operator, least-square estimation is used. This implies, in the experiment, the nonlinearity of the trajectory of the leader robot would affect the accuracy of the velocity prediction algorithm. Regarding track one, the external potential primarily affects movement along the v-axis. Furthermore, due to the symmetry of the external potential, this effect along the v-axis is similar for both the leader and follower robots. Consequently, as the predefined velocity of the leader robot remains constant, the trajectory of the follower robot follows a nearly linear path. In contrast, for track two, the trajectories of the leader and follower robots are situated in different regions of the external potential, causing varying effects of curvature. The follower robot's trajectory in track two is more nonlinear than in track one due to the curvature of the external potential. This disparity in trajectory nonlinearity can explain the discrepancy in the effectiveness of DMD velocity prediction between tracks one and two.

### 5.2.2 On limitations

An objective of the current experiment is to identify its limitations and possible areas for improvement.

**Mobility** Due to its weight, the robot struggles to execute precise velocity movements in regions of the external potential where the curvature is greater. This under-performance would negatively impact both the visual algorithm for positioning correction and the velocity prediction algorithm. To improve the robot’s mobility, reducing the overall weight and implementing PID control could be potential solutions.

**Communication delay** In the experiment presented in this paper, the leader robot waited for the follower robot to reach the desired position before moving for each given time step. As the scale of the formation increases, this waiting time would also increase.

**Visual system error** The visual system utilized in the experiment employs Pixy2 for image recognition. The sensitivity of Pixy2 directly impacts the accuracy of the visual algorithm. The experiment’s visual algorithm requires a high level of sensitivity, which inevitably leads to image data reading errors due to flickering. For future work, alternative sensing methods could be considered.

## 6 Conclusion

In this paper, we validated our theoretical formulation of the formation control algorithm using mobile robots. Specifically, we designed and tested two omnidirectional mobile robots in a nonlinear two-dimensional elliptic paraboloid external potential. During the experiment, the formation control algorithm for the follower robot incorporated a velocity prediction algorithm using DMD, a visual algorithm for position correction, and a movement algorithm for the robot’s mobility. Our results indicate that the algorithm successfully maintained the desired formation for the follower robot.

The algorithm with DMD velocity prediction decreases the workload for position correction by the visual algorithm, which, in turn, increases the efficiency of the overall formation control. However, the DMD velocity prediction algorithm outperforms the algorithm without DMD prediction if the trajectory of the follower robot is nonlinear, while there is no significant difference for trajectories that are close to linear.

Improvements can be made to the robot’s mobility and visual system to increase its performance. For future work, we envisage experimenting with a larger formation on the nonlinear external potential, and also verifying the formation analysis algorithm in [18] through experiment.

## Acknowledgments

Y.W and T.H acknowledges Professor H. Arai and N. Satoh from Chiba Institute of Technology for helpful discussions. Y.W is supported by the Japanese Government MEXT Scholarship Program.

## 7 References

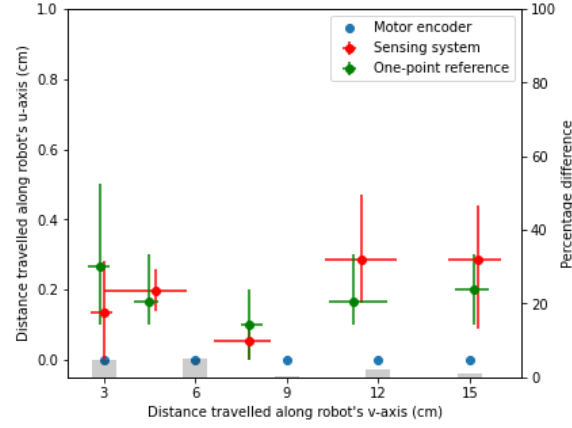
### References

- [1] Alessandro Attanasi, Andrea Cavagna, Lorenzo Del Castello, Irene Giardina, Tomas S. Grigera, Asja Jelić, Stefania Melillo, Leonardo Parisi, Oliver Pohl, Edward Shen, and Massimiliano Viale. Information transfer and behavioural inertia in starling flocks. *Nature Physics*, 10(9):691–696, 2014.
- [2] Veysel Gazi and Barış Fidan. Coordination and control of multi-agent dynamic systems: models and approaches, 2006.
- [3] Ugo Lopez, Jacques Gautrais, Iain D. Couzin, and Guy Theraulaz. From behavioural analyses to models of collective motion in fish schools. *Interface Focus*, 2(6):693–707, 2012.
- [4] David Mateo, Nikolaj Horsevad, Vahid Hassani, Mohammadreza Chamanbaz, and Roland Bouffanais. Optimal network topology for responsive collective behavior. *Science Advances*, 5(4):eaau0999, 2019.
- [5] Reza Olfati-Saber. Flocking for multi-agent dynamic systems: algorithms and theory. *IEEE Transactions on Automatic Control*, 51:401–420, 2006.
- [6] Tamás Vicsek and Anna Zafeiris. Collective motion. *Physics Reports*, 517(3):71–140, 2012.
- [7] Jianing Chen, Melvin Gauci, Wei Li, Andreas Kolling, and Roderich Groß. Occlusion-based cooperative transport with a swarm of miniature mobile robots. *IEEE Transactions on Robotics*, 31(2):307–321, 2015.
- [8] K. N. McGuire, C. De Wagter, K. Tuyls, H. J. Kappen, and G. C. H. E. de Croon. Minimal navigation solution for a swarm of tiny flying robots to explore an unknown environment. *Science Robotics*, 4(35):eaaw9710, 2019.
- [9] Joan Saez-Pons, Lyuba Alboul, Jacques Penders, and Leo Nomdedeu. Multi-robot team formation control in the guardians project. *Industrial Robot: An International Journal*, 2010.
- [10] Siwei Zhang, Robert Pöhlmann, Thomas Wiedemann, Armin Dammann, Henk Wymeersch, and Peter Adam Hoehner. Self-aware swarm navigation in autonomous exploration missions. *Proceedings of the IEEE*, 108(7):1168–1195, 2020.

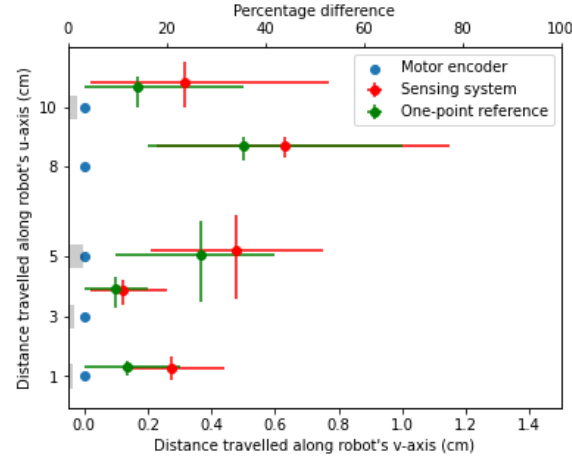
- [11] Ali Marjovi and Lino Marques. Optimal swarm formation for odor plume finding. *IEEE Transactions on Cybernetics*, 44(12):2302–2315, 2014.
- [12] Craig W. Reynolds. Flocks, herds and schools: A distributed behavioral model. In *Proceedings of the 14th Annual Conference on Computer Graphics and Interactive Techniques*, SIGGRAPH '87, page 25–34, New York, NY, USA, 1987. Association for Computing Machinery.
- [13] Ali Emre Turgut, Hande Çelikkanat, Fatih Gökçe, and Erol Sahin. Self-organized flocking in mobile robot swarms. *Swarm Intelligence*, 2:97–120, 2008.
- [14] Toshiyuki Yasuda, Akitoshi Adachi, and Kazuhiro Ohkura. Self-organized flocking of a mobile robot swarm by topological distance-based interactions. In *2014 IEEE/SICE International Symposium on System Integration*, pages 106–111, 2014.
- [15] Florian Berlinger, Melvin Gauci, and Radhika Nagpal. Implicit coordination for 3d underwater collective behaviors in a fish-inspired robot swarm. *Science Robotics*, 6(50):eabd8668, 2021.
- [16] Rattanachai Ramaithitima, Michael Whitzer, Subhrajit Bhattacharya, and Vijay Kumar. Automated creation of topological maps in unknown environments using a swarm of resource-constrained robots. *IEEE Robotics and Automation Letters*, 1(2):746–753, 2016.
- [17] Hung Manh La and Weihua Sheng. Distributed sensor fusion for scalar field mapping using mobile sensor networks. *IEEE Transactions on Cybernetics*, 43(2):766–778, 2013.
- [18] Yanran Wang and Takashi Hikiyara. Two-dimensional swarm formation in time-invariant external potential: Modeling, analysis, and control. *Chaos: An Interdisciplinary Journal of Nonlinear Science*, 30(9):093145, 2020.
- [19] Alexandre Mauroy, Igor Mezic, and Yoshihiko (Eds.) Susuki. *The Koopman Operator in Systems and Control Concepts, Methodologies, and Applications: Concepts, Methodologies, and Applications*. 01 2020.
- [20] S.L. Brunton and J.N. Kutz. *Data-Driven Science and Engineering: Machine Learning, Dynamical Systems, and Control*. Cambridge University Press, Cambridge, England, 2019.
- [21] Yoshihiko Susuki, Igor Mezic, Fredrik Raak, and Takashi Hikiyara. Applied koopman operator theory for power systems technology. *Nonlinear Theory and Its Applications, IEICE*, 7(4):430–459, 2016.
- [22] Hao Zhang, C.W. Rowley, E.A. Deem, and L.N. Cattafesta. Online dynamic mode decomposition for time-varying systems. *SIAM Journal on Applied Dynamical Systems*, 18(3):1586–1609, 2019.



- [23] John M. Lee. *Riemannian Manifolds: An Introduction to Curvature*. Springer-Verlag New York, Inc., New York, USA, 1997.
- [24] Vladimir G. Ivancevic and Tijana T. Ivancevic. *Applied Differential Geometry: A Modern Introduction*. World Scientific Publishing Co. Pte. Ltd., Singapore, 2007.
- [25] Olaf Diegel, Aparna Badve, Glen Bright, Johan Potgieter, and Tlale Sylvester. Improved mecanum wheel design for omni-directional robots. In *2002 Australasian Conference on Robotics and Automation*, pages 117–121, 2002.



(a)



(b)

Figure 7: Travelled distances comparison. Various travelling distances are pre-set and converted into wheel rotations according to robot's individual motor calibration functions. Travelled distance measured by motor encoder, by sensing system, and by one-point reference method is in blue, red, and green, respectively. Gray bar represents the percentage difference of measured distance between sensing system and one-point reference method. (a) Travelling along v-axis. (b) Travelling along u-axis.

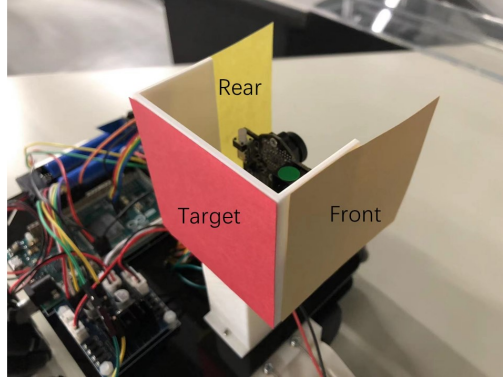


Figure 8: View of the robot's visual system.

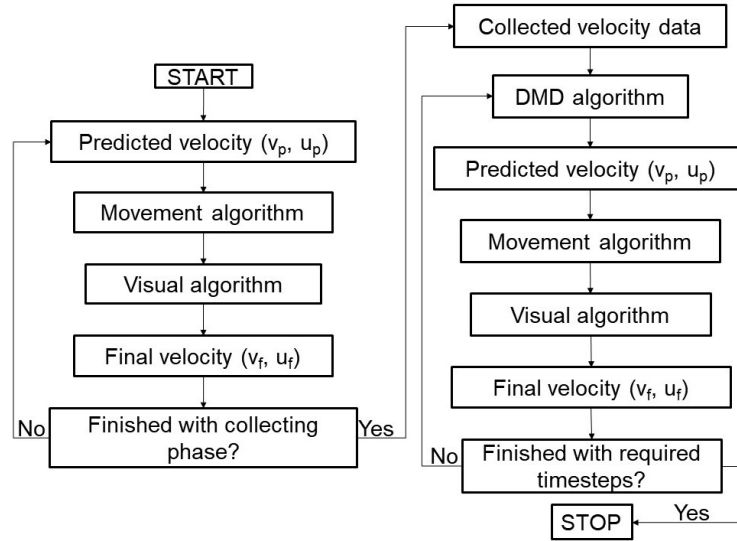


Figure 9: The overall algorithm scheme for follower robot. In the main algorithm, there is three sub-algorithm: movement algorithm, visual algorithm, and velocity prediction algorithm.

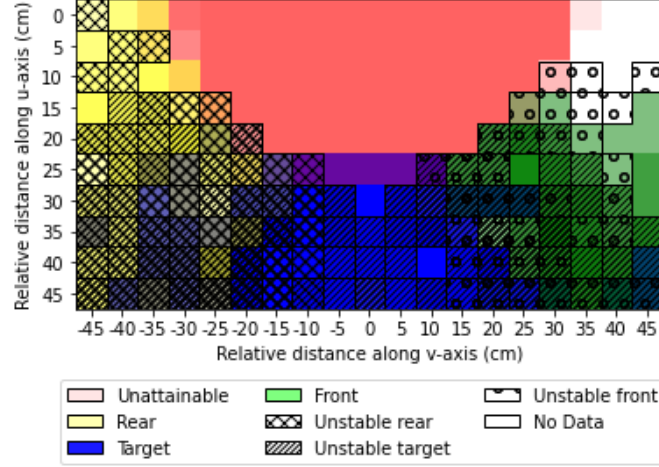


Figure 10: Pixy2 captured images with respect to relative position. All relative angles are overlaid. The overlap between Unattainable area and other areas is due to different relative angles. This overlap do not affects the design of the visual algorithm.

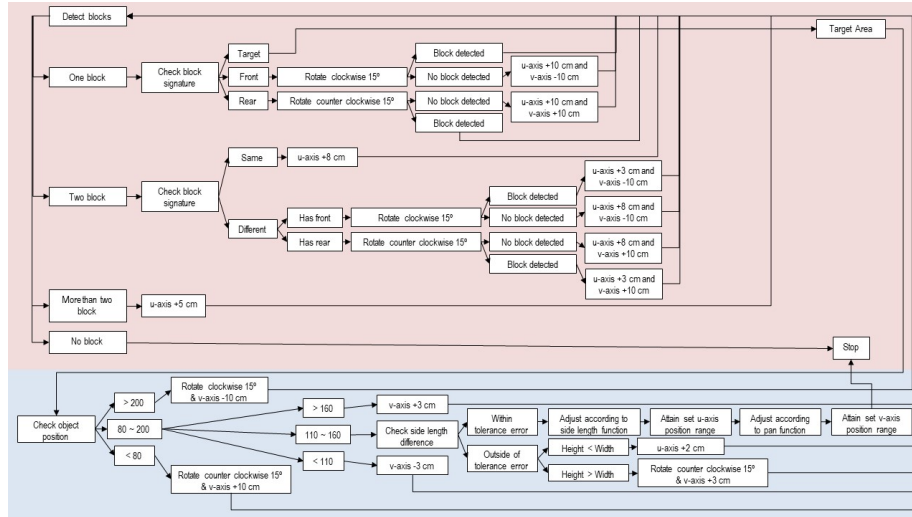


Figure 11: Visual algorithm flow for entering Target area in purple. Visual algorithm flow for obtaining ideal position while in Target area in red.

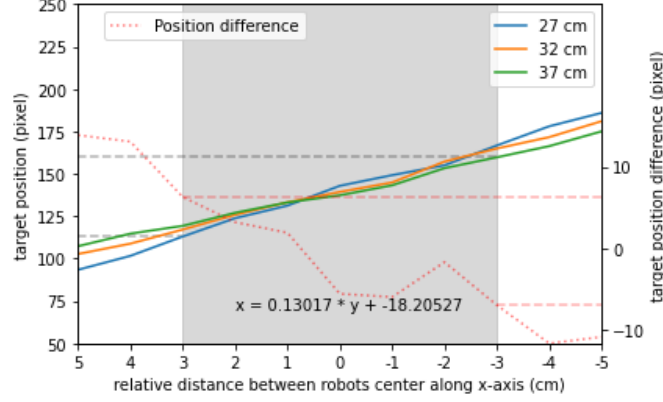


Figure 12: Relative distance along v-axis verse Target color signature block position. Blue, orange, and green lines represent different relative distance between robots along u-axis. The red dotted line represents the maximum difference in Target color signature block position for various relative distance along u-axis. Gray area,  $(-3, 3)$  cm represent finetuning area. Inside the finetuning area, the maximum difference in Target color signature block position for various relative distance along u-axis is less than 7 pixels. The finetuning area corresponds to Target color signature block position range 110 – 160, shown in horizontal dotted gray lines.

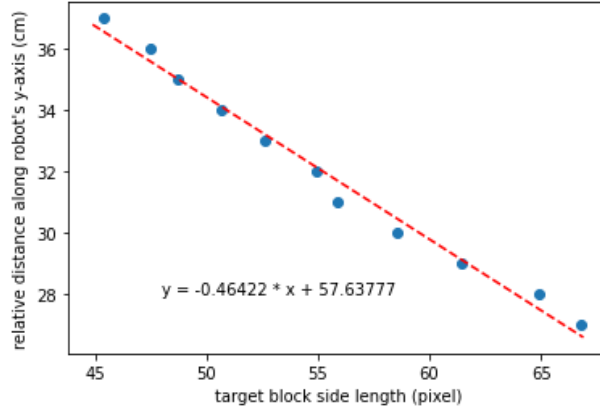


Figure 13: Target block side length verses relative distance along u-axis with zero relative distance along v-axis and zero relative angle.

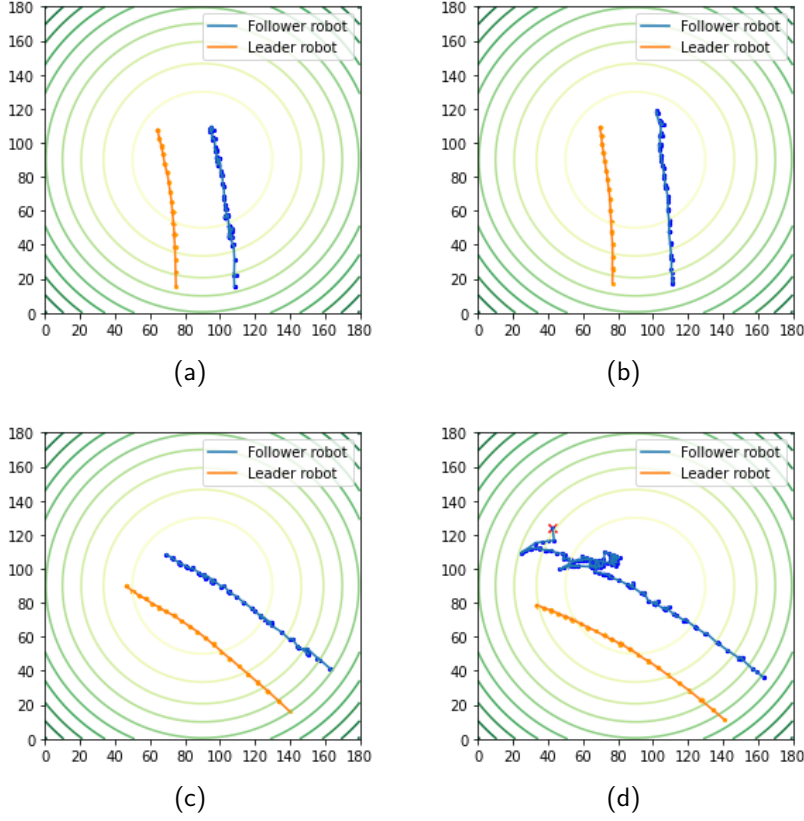
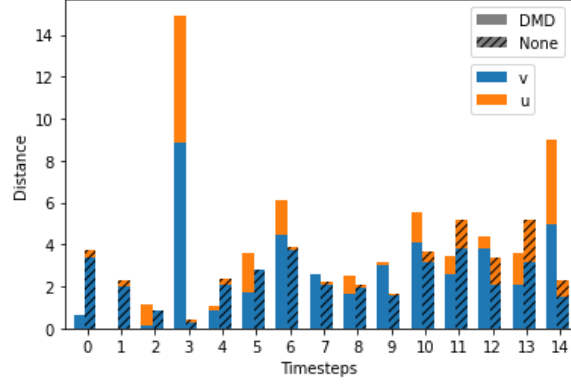
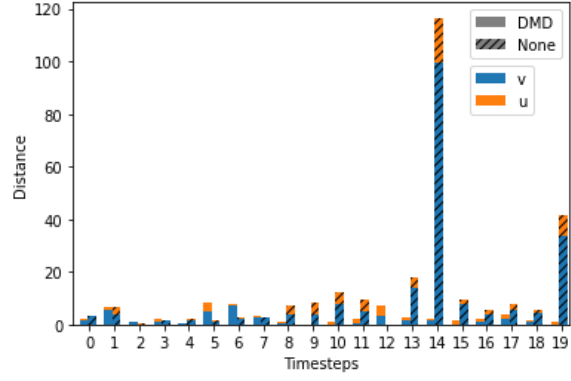


Figure 14: Trajectory of the leader robot and follower robot in elliptic paraboloid external potential. The trajectory of the leader robot is represented in orange, while the trajectory of the follower robot is depicted in blue. The green contour line in the background represents the external potential. All robots have initial velocity 5 cm per given timestep. Red cross mark indicates that the follower robot have lost the visual of its beacon neighbour (the leader robot). (a) Track one with DMD velocity prediction algorithm. Initial position of the leader robot is at (76.3, 15.8) cm. Error due to camera distortion is at maximum of 1.3 cm. (b) Track one without DMD velocity prediction algorithm. Initial position of the leader robot is (76.9, 17.3) cm. Error due to camera distortion is at maximum of 1.7 cm. (c) Track two with DMD velocity prediction algorithm. Initial position of the leader robot is (141.2, 11.1) cm. Error due to camera distortion is at maximum of 1.7 cm. (d) Track two without DMD velocity prediction algorithm. Initial position of the leader robot is (139.7, 16.3) cm. Error due to camera distortion is at maximum of 2.7 cm.



(a)



(b)

Figure 15: Correction distance comparison between DMD prediction algorithm and Non-DMD prediction algorithm for (a) track one and (b) track two. For each timestep, distance travelled in v-axis (blue) and u-axis (orange) of robot are recorded for both DMD prediction and Non-DMD prediction algorithm (striped).

## A Differential geomtry

Let  $U \subseteq \mathbb{R}^n$  be a non-empty open subset and  $F : U \rightarrow \mathbb{R}$  a  $C^\infty$  function defining the external potential. Let  $M \subseteq U \times \mathbb{R}$  be the graph of  $f$ . The closed subset  $M$  in  $U \times \mathbb{R}$  projects homeomorphically onto  $U$  with inverse  $(x_1, \dots, x_n) \mapsto (x_1, \dots, x_n, F(x_1, \dots, x_n))$  that is a smooth mapping from  $U$  to  $U \times \mathbb{R}$ .  $M$  is a closed smooth submanifold of  $U \times \mathbb{R}$ . Using the standard Riemannian metric on  $U \times \mathbb{R} \subseteq \mathbb{R}^{n+1}$ , the induced metric  $g$  on  $M$  at a point  $p \in M$  is

$$g(p) = \langle \partial_{q_i}|_p, \partial_{q_j}|_p \rangle_p dq_i(p) \otimes dq_j(p) \quad (9)$$

with coordinate chart  $\{q_i\}$  on  $M$ . Each  $\partial_{q_i}|_p \in T_p M$  can be represented as a linear combination of  $\{\partial_{x_i}|_p\} \in T_p(\mathbb{R}^{n+1})$ , given as

$$\partial_{q_i}|_p = \partial_{x_i}|_p + \partial_{x_i} f(p) \partial_{x_{n+1}}|_p. \quad (10)$$

Consider the aforementioned graph  $M$  as a  $C^\infty$  Riemannian manifold. Given a curve,  $C : [a, b] \rightarrow M$ , a *vector field*  $X$  along  $C$  is any section of the tangent bundle  $TM$  over  $C$  ( $X : [a, b] \rightarrow TM$ , projection  $\pi : TM \rightarrow M$ , such that  $\pi \circ X = C$ ). If  $M$  is a smooth manifold, all vector field on the manifold are also smooth. We denote the collection of all smooth vector fields on manifold  $M$  as  $\mathfrak{X}(M)$ . For a Riemannian manifold  $(M, g)$ , the *Levi-Civita connection*  $\nabla_g$  on  $M$  is the unique connection on  $TM$  that has both metric compatibility and torsion freeness. The Christoffel symbols of the second kind are the connection coefficients (in a local chart) of the Levi-Civita connection denoted as

$$\Gamma_{bc}^a = \frac{1}{2} g^{ad} (\partial_c g_{db} + \partial_b g_{dc} - \partial_d g_{bc}). \quad (11)$$

For a Riemannian manifold  $(M, g)$ , a curve is called *geodesic* with respect to the connection  $\nabla_g$  if its acceleration is zero. That is a curve  $\gamma$  where  $\nabla_{\dot{\gamma}} \dot{\gamma} = 0$ . A geodesic curve in  $n$ -dimensional Riemannian manifold can be expressed as a system of second order ordinary differential equations,

$$\frac{d^2 \gamma^\lambda}{dt^2} + \Gamma_{\mu\nu}^\lambda \frac{d\gamma^\mu}{dt} \frac{d\gamma^\nu}{dt} = 0. \quad (12)$$

All geodesics are the shortest path between any two points on the manifold.



## B External potential specification

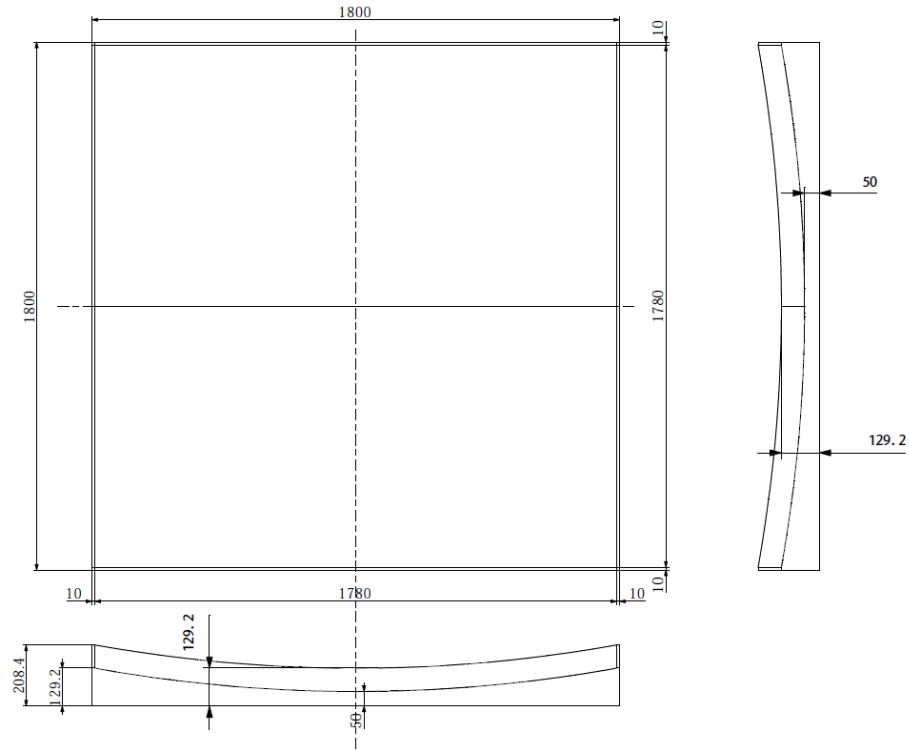


Figure 16: Specification of external potential. All units in mm.

## C Pixy2 parameters

Table 1: Pixy2 paramter settings

Parameter names	Values
Target signature range	5.0
Front signature range	6.0
Rear signature range	6.0
Camera brightness	100
Block filtering	40
Max merge distance	4
Min block area	20
Signature teach threshold	5600
LED brightness	4960
Auto exposure correction	On
Auto white balance	On
Flicker avoidance	On
Mininum frames per second	30

## D Pixy2 error

Table 2: Pixy2 error tolerance for visual algorithm

Data names	Tolerance values
Side length difference	4 pixel
v-axis position	5 pixel
u-axis position	1.5 cm

## E Online Dynamic Mode Decomposition

Using (8) in Section 4, we have

$$\mathbf{T}_k = \mathbf{B}_k \mathbf{A}_k^T (\mathbf{A}_k \mathbf{A}_k^T)^{-1}. \quad (13)$$

We define two new matrices  $\mathbf{P}_k$  and  $\mathbf{Q}_k$ ,

$$\mathbf{Q}_k = \mathbf{B}_k \mathbf{A}_k^T, \mathbf{P}_k = (\mathbf{A}_k \mathbf{A}_k^T)^{-1}, \quad (14)$$

so that  $\mathbf{T}_k = \mathbf{Q}_k \mathbf{P}_k$ .  $\mathbf{P}_k$  is well-defined if we ensure  $\mathbf{A}_k \mathbf{A}_k^T$  is invertible. The operator  $\mathbf{T}$  at time  $t_{k+1}$  is related to  $\mathbf{T}_k$  as

$$\begin{aligned} \mathbf{T}_{k+1} &= \mathbf{Q}_{k+1} \mathbf{P}_{k+1} \\ &= (\mathbf{Q}_k + \mathbf{b}_{k+1} \mathbf{a}_{k+1}^T) (\mathbf{P}_k^{-1} + \mathbf{a}_{k+1} \mathbf{a}_{k+1}^T)^{-1}. \end{aligned} \quad (15)$$

Using Sherman-Morrison formula, we can express  $\mathbf{P}_{k+1}$  as

$$\begin{aligned}\mathbf{P}_{k+1} &= (\mathbf{P}_k^{-1} + \mathbf{a}_{k+1}\mathbf{a}_{k+1}^T)^{-1} \\ &= \mathbf{P}_k - \frac{\mathbf{P}_k\mathbf{a}_{k+1}\mathbf{a}_{k+1}^T\mathbf{P}_k}{1 + \mathbf{a}_{k+1}^T\mathbf{P}_k\mathbf{a}_{k+1}}.\end{aligned}\tag{16}$$

$\mathbf{P}_{k+1}$  can be updated more efficiently, without the computation of inverses. Combining (16) and (15), we obtain the formula

$$\mathbf{T}_{k+1} = \mathbf{T}_k + \frac{(\mathbf{b}_{k+1} - \mathbf{T}_k\mathbf{a}_{k+1})\mathbf{a}_{k+1}^T\mathbf{P}_k}{1 + \mathbf{a}_{k+1}^T\mathbf{P}_k\mathbf{a}_{k+1}}.\tag{17}$$

$\mathbf{T}_{k+1}$  is computed using  $\mathbf{T}_k$  and new data pair  $\{\mathbf{a}_{k+1}, \mathbf{b}_{k+1}\}$ .